Dalton Transactions

ROYAL SOCIETY OF CHEMISTRY

PAPER

View Article Online
View Journal | View Issue

Cite this: *Dalton Trans.*, 2025, **54**, 6103

Probing structural defects and X-ray induced persistent luminescence mechanisms on rare earth-doped strontium sulfide materials†

Karina T. Fonseca,[a] Danilo O. A. Santos,[a] Fernando A. Garcia[b] and Lucas C. V. Rodrigues *[a]

Persistent luminescence is related to the existence of point defects in the crystal structure, which can be induced by the insertion of dopant ions to create trap levels for charge carriers. Strontium sulfide (SrS) is a promising host for X-ray activated phosphors due to its high luminescence yield and X-ray absorption efficiency. While the mechanisms of UV- and visible light-induced luminescence in rare-earth doped SrS have been previously explored, this work focuses on understanding X-ray induced mechanisms using synchrotron radiation techniques. Extended X-ray absorption fine structure (EXAFS) analysis suggested that rare-earth ions incorporate into the SrS lattice primarily as substitutional defects, with structural distortions depending on the differences in ionic radii between Sr^{2+} and $RE^{2+/3+}$. X-ray absorption near edge structure (XANES) spectra revealed the mixed-valence nature of Ce in SrS:Ce and SrS:Eu,Ce materials, and also that X-ray irradiation triggers complex charge transfer processes. The X-ray excited optical luminescence (XEOL) results showed that co-doped samples exhibited longer persistent luminescence decay times than their single-doped counterparts due to the increased number of defects. These findings provide new insights into the interplay between crystal defects and persistent luminescence in X-ray-activated phosphors, contributing to the design of more efficient materials for applications such as medical imaging, optical information storage, and industrial sensing.

Received 23rd October 2024,
Accepted 28th February 2025

DOI: 10.1039/d4dt02969k

rsc.li/dalton

1. Introduction

Point defects in crystalline materials govern a range of electrical, optical and mechanical properties.[1] Impurities, such as dopant ions or foreign atoms, can introduce additional defect sites that may alter the electronic structure of the material. Such changes lead to the creation of new energy levels that can trap charge carriers and are commonly used to tailor the luminescence properties of materials for specific applications, enhancing their efficiency.

Persistent luminescent materials emit light over long periods of time after the excitation source has been removed.[2] The mechanism that drives persistent luminescence consists of a gradual release of charge carriers from trapping centers, which are directly associated with lattice defects in a material. These charge carriers, then, recombine at the luminescent center, leading to significantly longer than expected luminescence lifetimes.[3,4]

Among diverse systems, alkaline earth sulfides are suitable host lattices for luminescent materials. These hosts are thermally stable and accessible and promote good sensitization of lanthanide ions, thus yielding high luminescence efficiency.[5] SrS is a highly efficient host for persistent luminescent materials and also a potential X-ray absorber, which favors X-ray induced optical (persistent) luminescence. Doped strontium sulfide has been studied with the aim to optimize its photonic properties and commercial viability for various industrial and technological applications.[6] SrS:Yb^{2+} (ref. 7), SrS:Eu^{2+},Dy^{3+} (ref. 8) and SrS:Eu^{2+},Pr^{3+} (ref. 9) have been explored, especially to expand the possibilities of persistent luminescence in the red and near infrared regions, with excitation in the UV-visible range. The effects of the nanostructure in SrS:Ce^{3+},Sm^{3+} materials on the improvement of their luminescence properties were also investigated,[10] as well as the occurrence of photoluminescence (PL), optical stimulated luminescence (OSL) and radioluminescence (RL), with their probable mechanisms suggested. Persistent luminescence mechanisms related to excitation by UV or visible radiation for SrS:Eu^{2+},Sm^{3+} have also already been proposed.[11] However, the

[a]Department of Fundamental Chemistry, Institute of Chemistry, University of São Paulo, São Paulo-SP, 05508-000, Brazil. E-mail: lucascvr@iq.usp.br
[b]Department of Applied Physics, Institute of Physics, University of São Paulo, São Paulo-SP, 05508-900, Brazil

† Electronic supplementary information (ESI) available. See DOI: https://doi.org/10.1039/d4dt02969k

processes occurring under X-ray exposure remain insufficiently understood, particularly for single-doped compounds such as SrS:Eu^{2+}, SrS:Ce^{3+}, and SrS:Sm^{3+}. A deeper investigation is needed to provide solid evidence on how the X-ray absorption of individual rare-earth dopants affects emission intensities and persistence. This work aims to address these gaps.

Recently, X-rays have been used as charging light in various materials. Rare earth activated scintillators have been investigated in the search for more efficient materials for medical imaging, optical information storage, safety and industrial applications.[12–15] Recent studies on X-ray persistent phosphors have been primarily focusing on biological applications, such as bioimaging and photodynamic therapy (PDT). Persistent luminescence, at first, has received significant attention for its role in enhancing signal-to-noise ratios and enabling continuous tracking in bioimaging without the need for an external excitation source. However, its application in living systems has been constrained by two major challenges: the short observation times and the limited tissue penetration depth of conventional UV-visible excitation light required to activate persistent luminescence *in vivo*. To overcome these issues, X-ray-activated persistent luminescence nanomaterials are being investigated in several works. For instance, ZnS:Cu^{2+},Co^{2+} nanoparticles were conjugated to the photosensitizer tetrabromorhodamine-123 (TBrRh123) and their persistent emission successfully activated TBrRh123 for PDT. This approach not only significantly reduced the required radiation dose but also demonstrated effective cytotoxicity against PC3 human prostate cancer cells.[16] Song and collaborators[17] have used an alternative strategy to design X-ray-excitable PDT systems. They demonstrated that a photosensitizer, such as zinc(II) phthalocyanine tetrasulfonic acid ($ZnPcS_4$), can be covalently conjugated to $ZnGa_2O_4$:Cr^{3+} (ZGO) persistent luminescence nanoparticles, resulting in a photodynamic therapy system (ZGO:Cr/$ZnPcS_4$). Notably, after cessation of X-ray irradiation, the persistent luminescence emitted by ZGO continues to activate the photosensitizer, thereby reducing the required X-ray dosage and minimizing the associated side effects of X-ray treatments. Furthermore, in the medical field, bioimaging capabilities can be significantly enhanced by utilizing probes that emit in the biological window I (650–980 nm) or nanoparticles emitting in the biological window II (1000–1600 nm). These emission ranges enable deeper tissue imaging and provide higher spatial resolution, making them particularly advantageous for advanced imaging techniques.[18] Photoclick chemistry is also another application where X-ray activated persistent phosphors, such as Gd^{3+}-doped $NaYF_4$, are of interest, since sustained high-energy output is required to drive the formation of covalent bonds.[19] Beyond their applications in biology, luminescent phosphors activated by X-rays offer a wide range of potential uses, including anti-counterfeiting, information storage, security, cryopreservation, and photocatalysis, which still requires further investigation.[14]

Regarding the experimental scope, the studies on X-ray induced persistent luminescence focus on understanding the intensity of the luminescence response that occurs as the excitation energy is scanned through a core absorption edge. The combination of X-ray absorption near edge structure (XANES) and X-ray excited optical luminescence (XEOL) aims to elucidate the dependence of excitation and emission spectra on the X-ray energy employed, as well as the correlation between the absorption edge and the excitation processes in the materials. Given that X-ray absorption spectroscopy (XAS) is an element-selective technique, this approach enables the identification of specific atoms contributing to the X-ray excited emission mechanism.[20]

Given the role of extrinsic defects in driving the emission of many persistent luminescent materials—such as strontium sulfide—the exact nature of the defect formed by the incorporation of rare earth elements into the crystal structure remains unresolved. Both substitutional and interstitial defects are plausible, depending on the lattice parameters and the ionic radius of the dopant. In this work, EXAFS analysis was employed to investigate and propose the occurrence of substitutional defects in rare-earth-doped SrS matrices. XANES and XEOL measurements were also conducted to investigate electronic processes triggered by X-ray excitation, such as changes in valence states and the radiative recombination of charge carriers. This study provides new insights and perspectives for advancing research on X-ray-induced persistent luminescence in rare-earth-doped sulfide hosts.

2. Experimental

2.1 Synthesis using the microwave assisted solid-state (MASS) method

Polycrystalline SrS:1%$RE^{2+/3+}$ and SrS:1%Eu^{2+},2%RE^{3+} materials (RE: Eu^{2+}, Sm^{3+} and Ce^{3+}) were prepared as reported previously.[11] Stoichiometric proportions of the starting compounds Eu_2O_3 (CSTARM, 99.99%), Sm_2O_3 (CSTARM, 99.99%), CeO_2 (CSTARM, 99.99%), S (Sigma-Aldrich, 99.5%), and $SrSO_4$ were thoroughly mixed and ground on an agate mortar. Strontium sulfate was prepared by precipitation through the $SrCl_2$ (99.0% Synth) and sulfuric acid (98.0% Reagen) reaction. A sulfur excess of 10 mol% was also added to the precursor to obtain a high purity material. The precipitate was filtered, washed several times with distilled water and dried at 100 °C for 24 h.

In the MASS synthesis, 12 g of granular activated carbon (∅:1–2 mm, Synth) was used as the microwave susceptor and placed in an alumina crucible (50 cm^3). A second alumina crucible (5 cm^3) containing 0.5 g of the precursor powder mixture was surrounded by the susceptor inside the first crucible. Both crucibles were partially covered with an alumina lid and then placed into a cavity of aluminosilicate thermal insulation bricks. Finally, the precursor powder was irradiated in a domestic microwave oven (Electrolux MEF41, 2.45 GHz) using an adjusted program of 12 and 10 minutes at 100% and 90% power levels, respectively. The resulting material was gently ground on an agate mortar and the heating step was repeated following the same microwave oven program.[11]

2.2 Characterization

The crystal structure and phase purity of the materials were verified with synchrotron radiation X-ray powder diffraction (SR-XRD) measurements at the XRD1 beamline[21] at the Brazilian Synchrotron Light Laboratory (LNLS-CNPEM), with 2θ from 5° to 120° in the Debye–Scherrer setup, using 12 keV energy irradiation and a Mythen 24 k detector. Rietveld refinements were performed using GSAS II software.[22]

X-ray absorption near edge structure (XANES) studies were performed to verify the oxidation states, as well as to correlate the X-ray absorption processes with total luminescence intensity. XANES data were recorded in the fluorescence mode using a Ge 15 element fluorescence detector (Canberra) at the LNLS-CNPEM XAFS2 beamline,[23] at the Eu, Sm and Ce L_3-edges. The Sr L_3-edge and S K-edge were measured at the SXS beamline,[24] in the total electron yield mode. All measurements were performed at room temperature.

Extended X-ray absorption fine structure (EXAFS) measurements were recorded in the transmission mode at the XAFS2 beamline around the Sr K-edge. The EXAFS data were analyzed using multiple scattering theory as implemented by the Demeter platform.[25]

X-ray excited optical luminescence (XEOL) excitation and emission spectra were recorded at the SXS beamline, simultaneously with XANES measurements, around the Sr L_3-edge and S K-edge. XANES data were recorded using the total electron yield (TEY) while the XEOL excitation data were collected using a Hamamatsu photomultiplier R928 coupled with an optical fiber and a Keithley 6514 detector. XEOL emission spectra were collected using an Ocean Optics QE65000 spectrophotometer.

3. Results and discussion

3.1 Crystal structure and phase purity

Rare earth-doped strontium sulfide materials were successfully synthesized through MASS synthesis. In this process, a reducing atmosphere of CO (g) is generated from the oxidation of the microwave susceptor (granular carbon) during the heating process. In addition to the desired SrS matrix, $SrSO_4$ and $SrCO_3$ were also present in the obtained products. Surface oxidation and hydrolysis due to air humidity are the major responsible for sulfate impurities, whereas the CO (g) atmosphere during the synthesis process is partially converted to CO_2 (g), leading to strontium carbonate formation on the surface of the samples. Analogous to what has been proposed for oxysulfide matrices,[26] the formation of sulfate-type bonds may also occur during synthesis as microwave irradiation is progressively increased. In this context, surface oxidation of the particles within the furnace takes place, also contributing to the formation of sulfate species. Rietveld refinements for the SrS:$RE^{2+/3+}$ and SrS:Eu^{2+},RE^{3+} SR-XRD patterns converged properly (Fig. 1 exemplifies these results for SrS:Eu^{2+}. For the other samples, see Fig. S2–6†). The obtained values for R_p, R_{wp} and χ^2 parameters can be seen in Table 1. The SrS crystal structure is face-centered cubic ($Fm\bar{3}m$ space group), in which Sr^{2+} ions are located in octahedral sites surrounded by six sulfur atoms. The phase fraction values related to sulfate and carbonate impurities varied along the samples, and a minimum phase purity of 81% for the desired SrS was obtained.

The cell parameters for SrS, $SrSO_4$ and $SrCO_3$ obtained from Rietveld refinements are also consistent with those reported in the literature.[27–29] The cell volume, as well as the lattice constant, remained similar for all doped SrS materials. Rare-earth oxides and also possible rare-earth side products were not detected in these samples. Due to its low concentration and similar ionic radii compared to Sr^{2+}, rare earth dopants did not promote significant structural changes, able to be detected by SR-XRD, in the SrS host.

3.2 EXAFS analysis and doping effects

Crystal defects are regions in real space where the microscopic arrangement of ions differs from that of a perfect crystal. Defects in general can be classified into line, surface or punctual defects, the latter being of greater interest for persistent luminescence mechanisms. For doped materials, extrinsic defects are the major responsible for the creation of trap states

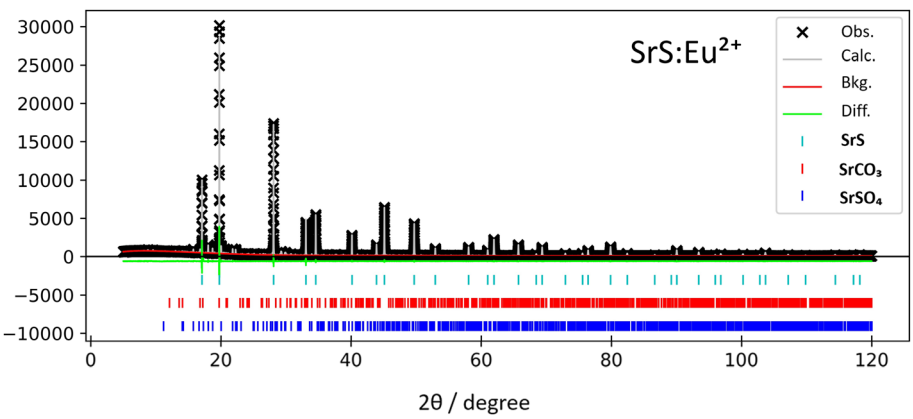

Fig. 1 SR-XRD patterns and Rietveld refinement for the SrS:Eu^{2+} material.

Table 1 Rietveld refinement results for strontium sulfide materials

	SrS:Eu^{2+}	SrS:Sm^{3+}	SrS:Ce^{3+}	SrS:Eu^{2+},Sm^{3+}	SrS:Eu^{2+},Ce^{3+}
SrS fraction (wt%)	81.4	93.8	98.0	93.2	90.5
Lattice constant (Å)	6.01907	6.01901	6.01912	6.01914	6.01908
Cell volume (Å^3)	218.07	218.06	218.07	218.07	218.07
$SrSO_4$ fraction (%)	15.6	0.7	1.4	0.3	2.3
$SrCO_3$ fraction (%)	3.0	5.5	0.6	6.5	7.2
R_p (%)	7.93	6.26	9.23	8.502	9.02
R_{wp} (%)	6.50	5.08	6.64	5.56	5.36
χ^2	1.08	0.98	2.02	1.47	1.56

in the band structure, which can capture charge carriers and store energy from the incident radiation. In the co-doping of persistent luminescent materials, several compounds, such as $CaAl_2O_4$:Eu^{2+} and $SrMgSi_2O_7$:Eu^{2+}, have shown significant increases in persistence time, by up to four orders of magnitude, with the inclusion of RE^{3+} co-dopants.[30,31] However, in the case of SrS:Eu^{2+}, luminescence decay times remain similar across materials, regardless of the co-dopant, with the increase in persistence time being limited to a maximum of sixfold.[11] The application of EXAFS to the study of persistent luminescence, in this work, involves the investigation of the local structure of Sr in the doped SrS matrix, with the aim of finding a correlation between persistent luminescence decay time and disorder in the local atomic environment. The strontium atom is inside an octahedral site, surrounded by six sulfur atoms, and was chosen as the absorber.

Considering that there are different possibilities for the types of defects formed in the doped SrS matrix, some models were tested for the treatment of EXAFS spectra. Simulations included the entry of a $RE^{2+/3+}$ ion in the Sr^{2+} site, as a substitutional defect, with and without the formation of vacancies, at different distances from the absorber; and the insertion of $RE^{2+/3+}$ in the interstitial site of the SrS fcc structure.

The dimensions of the interstitial site are relevant to assess the possibility of dopant insertion. Considering its geometry, the fcc crystal structure exhibits tetrahedral interstitial sites (Fig. S1†), in which a dopant ion would be coordinated by four host atoms. The radius of the interstitial atom (r_i), however, may follow the relation $r_i = 0.225R$ with respect to the radius of the host atom (R), as discussed in section S1 of the ESI.† Cation dopants are supposed to be coordinated by four sulfide ligands (R = 1.840 Å (ref. 32)), so their radii must be on the order of 0.41 Å. Therefore, the interstitial site is considerably small to accommodate the insertion of a rare earth atom, and this hypothesis was discarded.

In this work, the model used for the treatment of EXAFS spectra supposes that the rare-earth dopant enters the site of strontium as a substitutional defect. This assumption is reasonable since the radii of Sr^{2+} and of $RE^{2+/3+}$ are relatively similar (1.180, 1.170, 1.020 and 1.010 Å for Sr^{2+}, Eu^{2+}, Sm^{3+} and Ce^{3+} with a coordination number of six, respectively[32]). The formation of vacancies, *i.e.*, the absence of a Sr^{2+} or S^{2-} ion in the SrS structure, was also tested considering charge compensation and the presence of Schottky defects, but it did not contribute to any changes in the quality of the obtained fits. Aiming to work with the simplest possible model, the doping situation is restricted to the entry of $RE^{2+/3+}$ in the Sr^{2+} site, without any other modification in the lattice. The position of the rare earth ion with respect to the absorber was also investigated.

The Fourier transform data for doped SrS materials are shown in Fig. 2b–f, as the real part of $\chi(R)$ concentrated in the region up to 6 Å from the absorber. FEFF calculations were performed over a cluster of 121 atoms, in which one Sr atom was replaced by a rare-earth atom (Eu, Sm or Ce) for single-doped SrS materials, and for co-doped structures, two Sr atoms were replaced by Eu and a second rare-earth atom (Sm or Ce). This procedure took into consideration the percentage of doping in the samples, which was 1% and 2% for single-doped and co-doped materials, respectively. Furthermore, the strontium atom chosen to be replaced was the one closest to the absorber (*i.e.* in the second coordination sphere). Replacing a Sr^{2+} ion with an $RE^{2+/3+}$ ion at greater distances does not contribute significantly to the EXAFS signal, making no difference to the fit. Therefore, all simulations associated the doping process with the entry of the rare earth ion in the site of a Sr^{2+} ion in the second coordination sphere.

Single and multiple scattering paths relating Sr and S, as well as a single scattering Sr–RE path, were adopted to describe the data, so Sr–S bonds and Sr–Sr and Sr–RE distances are investigated (Fig. 3).

The results obtained from the theoretical model provided the correlated Debye–Waller parameters (σ^2), corrected bond distances (R) and the α coefficient associated with each Sr–X interaction, seeking to compare the doping effects on the SrS host. The α coefficient represents the expansion or the contraction of bond lengths, thus acquiring positive or negative values. The bond distances are directly proportional to α, and in the model adopted for data processing, these variations were defined as

$$\Delta R = \alpha \times R_{\text{eff}}$$

where R_{eff} refers to the effective lengths for the particular scattering path considered. The correlated Debye–Waller parameters bring information on bond disorder, which contains a dynamic component, associated with the vibrations of the atoms in each bond (and is a function of temperature) and static components (associated with the defects present in the crystal lattice). The EXAFS analysis showed that the behavior of the σ^2 parameters for Sr–S and Sr–Sr bonds follows the trend of α: as

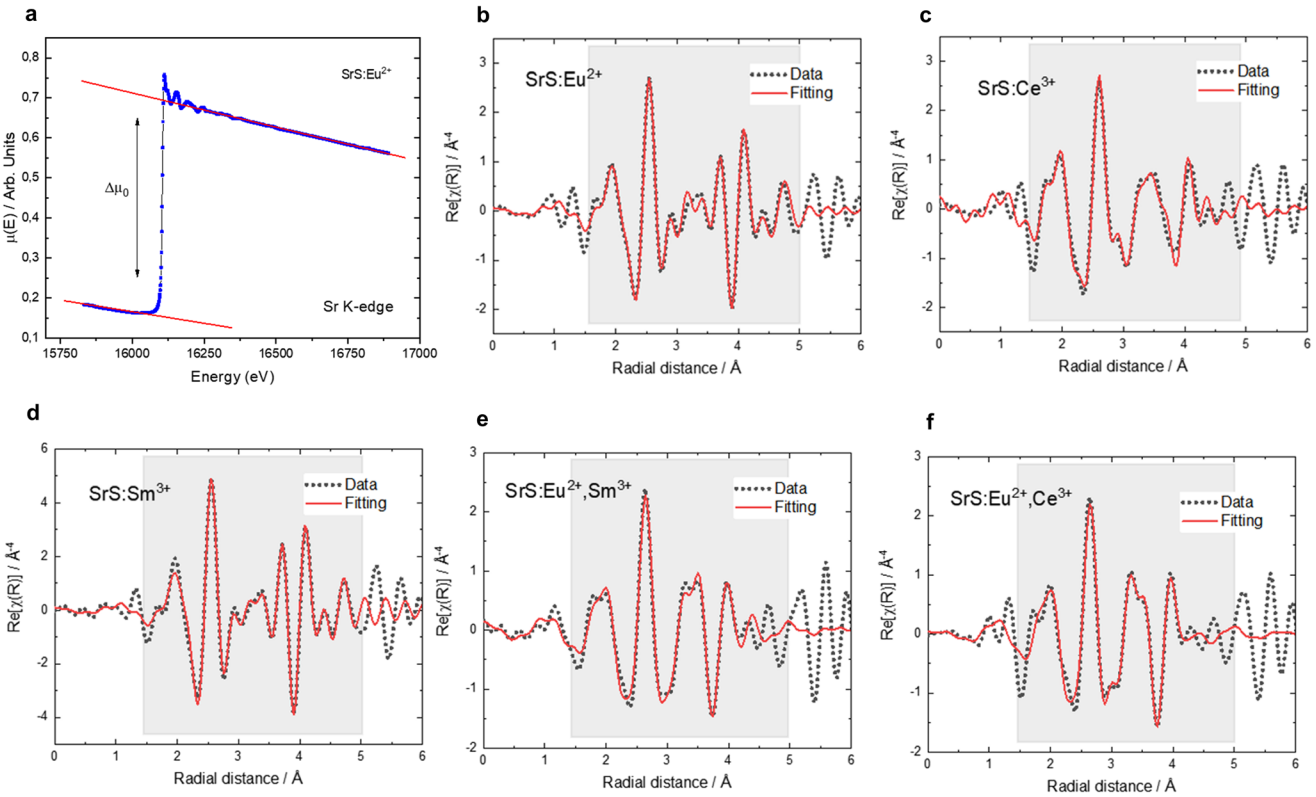

Fig. 2 (a) XAS spectra of SrS:Eu^{2+} at the Sr K-edge. (b–f) Fourier transform EXAFS spectra up to 6 Å from the absorber (dot line) and the theoretical model (solid red line), with the *R* window ranging from 1.5 to 5 Å (gray region).

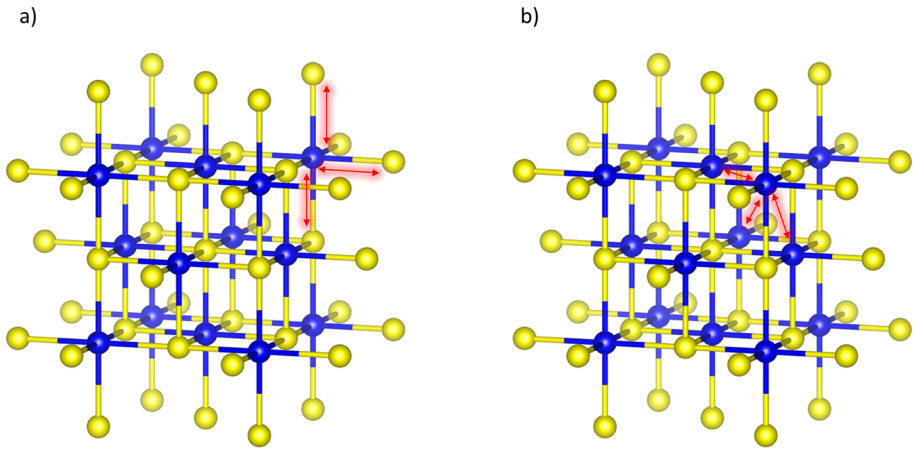

Fig. 3 Bond lengths probed using EXAFS spectra in the SrS crystal structure. Sr and S atoms are represented by blue and yellow balls, respectively. (a) Sr···S bonds and (b) Sr···Sr or Sr···RE distances.

co-dopants are added to the structure, we have greater variations in *R* values and an increase in the dispersion of Sr–X distances (Fig. 4a and b). Considering the single-doped materials, SrS:Ce^{3+} was the one with the highest values for α and σ^2 (Fig. 4c). Furthermore, a direct correlation was observed between α and the difference between the ionic radii of Sr^{2+} and $RE^{2+/3+}$: the greater the difference between the radii of Sr^{2+} and the rare earth substituent, the greater the parameters σ^2 and α (Fig. 4d), which indicates a greater potential for network distortion, as proposed in the literature.[33] The correlated Debye–Waller parameters, as well as the variations in Sr–X distances, obtained by analyzing the spectra of the five materials are listed in Tables 2 and 3.

The decreased Debye–Waller factor values in the EXAFS analysis of doped materials can arise from various factors, typically related to the local structural environment and experi-

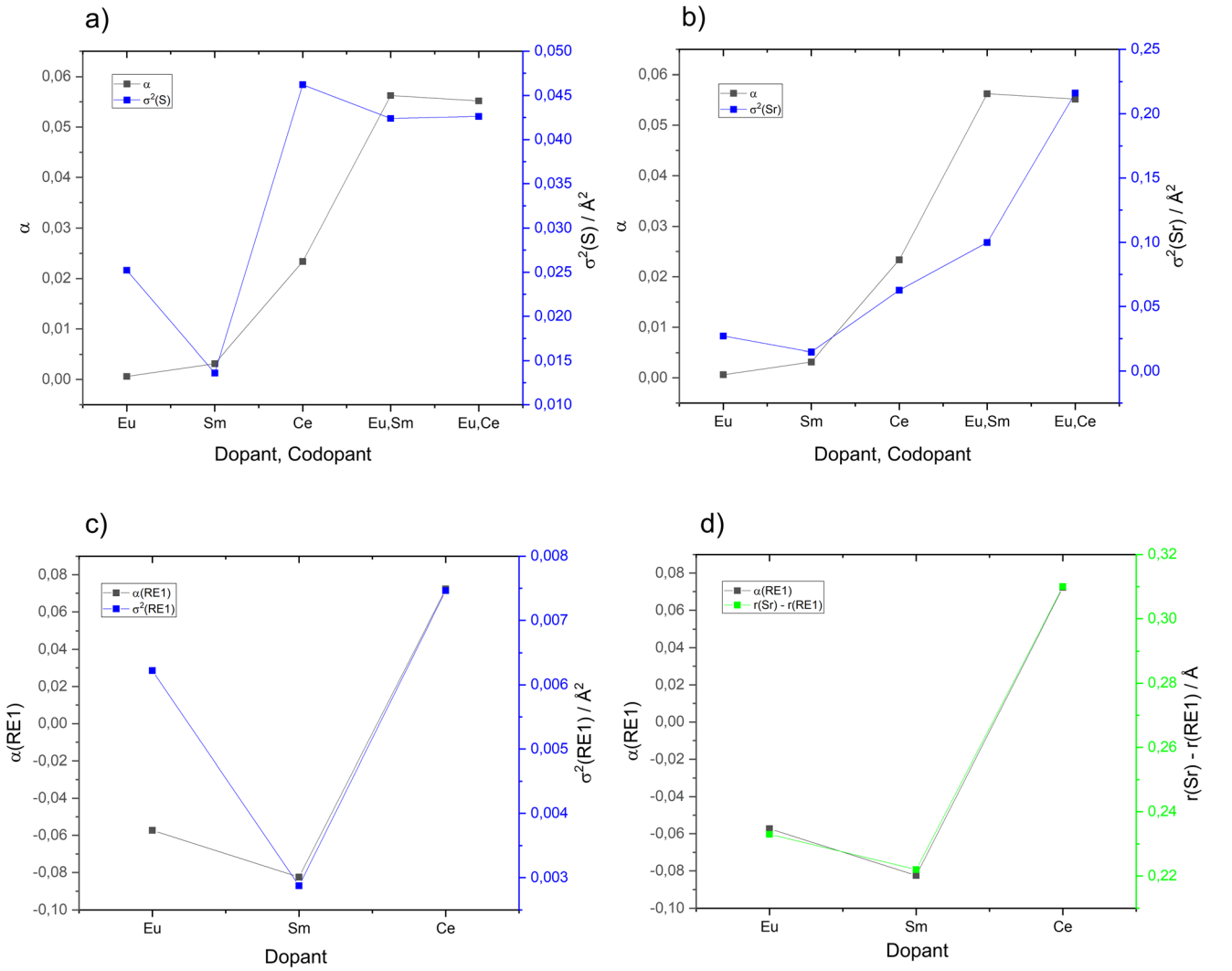

Fig. 4 (a–c) Comparison of Debye–Waller (σ^2) and α parameters for each Sr–X path (X = S, Sr, Eu, Sm, Ce) in SrS materials. (d) Relation between Sr–RE bond length variation and the difference in their crystal radii values.

Table 2 Variation in bond lengths in doped SrS materials. $S^{(1)}$ refers to a sulfide ligand in the first coordination sphere; RE1 and RE2 correspond to the dopant and co-dopant, respectively

Material	ΔR (Sr–$S^{(1)}$)/Å	ΔR (Sr–RE1)/Å	ΔR (Sr–RE2)/Å	ΔR (Sr–Sr)/Å
SrS:Eu^{2+}	0.0019 ± 0.0008	−0.2439 ± 0.0030	—	0.0026 ± 0.0005
SrS:Sm^{3+}	0.0095 ± 0.0008	−0.3509 ± 0.0020	—	0.0135 ± 0.0008
SrS:Ce^{3+}	0.0703 ± 0.0120	0.3079 ± 0.0080	—	0.0994 ± 0.0050
SrS:Eu^{2+},Sm^{3+}	0.1693 ± 0.0820	0.3521 ± 0.0085	0.1961 ± 0.0030	0.2394 ± 0.0120
SrS:Eu^{2+},Ce^{3+}	0.1665 ± 0.0950	0.2039 ± 0.0086	0.3519 ± 0.0086	0.2349 ± 0.0920

Table 3 Debye–Waller parameters related to each Sr–X path in doped SrS materials

Material	σ^2 (Sr–$S^{(1)}$)/Å^2	σ^2 (Sr–RE1)/Å^2	σ^2 (Sr–RE2)/Å^2	σ^2 (Sr–Sr)/Å^2
SrS:Eu^{2+}	0.025 ± 0.010	0.006 ± 0.001	—	0.027 ± 0.002
SrS:Sm^{3+}	0.014 ± 0.005	0.003 ± 0.001	—	0.015 ± 0.002
SrS:Ce^{3+}	0.046 ± 0.030	0.007 ± 0.002	—	0.063 ± 0.004
SrS:Eu^{2+},Sm^{3+}	0.042 ± 0.020	0.001 ± 0.0005	0.001 ± 0.0006	0.099 ± 0.008
SrS:Eu^{2+},Ce^{3+}	0.042 ± 0.020	0.001 ± 0.0006	0.001 ± 0.0006	0.216 ± 0.009

mental conditions. In this study, the σ^2 values for Sr–RE paths were generally much lower than those for the first-shell Sr–S paths. The most likely explanation is the higher atomic mass of the lanthanide dopant relative to sulfur, which reduces vibrational amplitudes and leads to lower σ^2 values. It is seen that for co-doped materials, the values of ΔR (and, consequently of α) are always positive for all bonds, indicating an increase in interatomic distances due to the presence of a greater number of defects. For single-doped materials, especially when the dopants are Eu^{2+} or Sm^{3+}, there is a contraction of the Sr–RE distances, compared to what was predicted based on the structure of the host and considering the entry of the dopant into the Sr^{2+} site, being represented by negative values of α and ΔR. Sr–$S^{(1)}$ bonds expanded in all materials, which is a consequence of the higher charge to radius ratio (Z/r) of $RE^{2+/3+}$ compared to Sr^{2+}, especially in the cases of Sm^{3+} and Ce^{3+}. In this context, the rare earth dopant attracts the sulfur atoms closer towards it, shortening the RE–S bond and stretching the Sr–$S^{(1)}$ bond.

XAS and XRD are sensitive to different features of the pair correlation function and thus are complementary in studying the same system, even in well-ordered crystalline materials. EXAFS provides details of the local structure that are inaccessible to the diffraction Bragg scattering contribution, which gives information on the average of the atomic arrangements.[34] Our analysis demonstrated structural changes that, at first, had not been detected by XRD. When we verified the lattice parameters, for all crystals, X-ray diffraction showed that the insertion of $RE^{2+/3+}$ into the SrS matrix maintained the integrity of the structure, without significant distortions. However, when locally probing the environment around a Sr atom, considerable punctual changes were observed due to the replacement of some atoms in the structure by $RE^{2+/3+}$. When simultaneously analyzing the increase in the background of XRD data and the elevated Debye–Waller factor values for Sr–S and Sr–Sr bonds, it is possible to infer the presence of amorphous impurities. The increase in the background at lower angles is often associated with the presence of amorphous phases, for which EXAFS is also sensitive. If only SrS and disordered SrS:RE phases were present, σ^2 values would be affected, but no changes would be detected in the XRD. In this context, $SrSO_4$ impurities are the most probable contribution to this amorphous phase. The model employed in this study constitutes a first approximation of the system, in which the EXAFS signal is assumed to originate exclusively from the SrS matrix in the absence of impurities. Nevertheless, the inclusion of Sr–O bonding contributions to the EXAFS signal could potentially enhance the model's accuracy, given the detected presence of $SrSO_4$ and $SrCO_3$ in the samples. However, considering the model's simplicity and the relatively low concentration of these impurities, their influence is not expected to compromise the reliability of the obtained results.

3.3 Oxidation states and luminescence studies

XANES measurements around the L_3-edges of rare earth dopants were performed for SrS:$RE^{2+/3+}$ and SrS:Eu^{2+},RE^{3+} materials, and also for rare earth standards. The oxidation states of the dopants were, initially, those related to the precursors (CeO_2, Eu_2O_3 and Sm_2O_3). Despite the use of a CO reducing atmosphere during the synthesis, in which the presence of Ce^{3+}, Eu^{2+} and Sm^{2+} is expected, both reduced and oxidized species are possibly present in all materials. In addition, the irradiation with X-rays creates free electrons that can be captured by Ln^{3+} to form Ln^{2+} in some hosts,[35] while the oxidation of Ln^{2+} is also a possible pathway when high energy radiation is applied. These behaviors demonstrate a certain complexity regarding the response of lanthanide doped materials to irradiation and compromise the reliability of the results obtained by XANES, which is discussed in this work.

Fig. 5a and b show the X-ray absorption spectra around the Ce L_3-edge for SrS:Ce and SrS:Eu,Ce materials. In these XANES spectra, A and B–C features are related to tetravalent and trivalent Ce oxidation states (mixed valence), respectively, while the D peak stands for the pre-edge region. Peaks B–C are related to transitions belonging to the $\underline{2p}4f^1\underline{L}5d^*$ final state (Ce^{3+}, where $\underline{2p}$ means a core hole in the $\underline{2p}$ level, $\underline{L}$ means a hole in the ligand and * means an excited electron). The A feature can be interpreted as a transition whose initial state is $2\underline{p}4f^15d^*$ + $\underline{2p}4f^05d^*$ (Ce^{4+}). Thus, A and B are related to $2p4f^0 \rightarrow \underline{2p}4f^05d^*$ and $2p4f^1\underline{L} \rightarrow \underline{2p}4f^1\underline{L}5d^*$ transitions, respectively.[36,37]

SrS:Ce and SrS:Eu,Ce materials both exhibit Ce mixed valence. The multivalent nature of lanthanides allows the occurrence of charge transfer processes between two nonequivalent lanthanide ions (metal-to-metal charge transfer – MMCT), as well as charge transfer processes between two equivalent metals (intervalence charge transfer – IVCT). The relative amounts of Ce^{3+} and Ce^{4+} were estimated by analyzing the peak areas of the four observed resonances, as indicated. In SrS:Ce XANES spectra (Fig. 5a), one can observe that the tetravalent ion is in higher concentration, while in SrS:Eu,Ce, the population of Ce^{3+} is predominant over Ce^{4+} (Fig. 5b), which indicates, as a first hypothesis, a possible $Eu^{2+} \rightarrow Ce^{4+}$ electron transfer process, once Eu^{3+} is observed at a higher concentration in the Eu L_3-edge XANES spectra (Fig. 5c). This process would consist of a photoinduced reversible reaction between Eu^{2+}–Ce^{4+} and Eu^{3+}–Ce^{3+} metastable states, as analogously reported for the $Eu^{2+/3+}$–$Sm^{2+/3+}$ pair in the CaF_2:Eu^{2+},Sm^{3+} material.[38]

$$Eu^{2+} + Ce^{4+} \leftrightharpoons Eu^{3+} + Ce^{3+}$$

The forward reaction can be observed when the SrS material is exposed to X-rays, while the backward reaction might occur under thermal excitation at room temperature. Electrons are assumed to be excited from the Eu^{2+} activator to the SrS conduction band and trapped by Ce^{4+}, forming metastable Ce^{3+} centers, where energy is stored. Then, thermal energy excites the trapped electrons from Ce^{3+} back to Eu^{3+} through the conduction band; the backtransferred electrons are then captured in an excited state of Eu^{2+}, which finally decays radiatively. In this system, however, Ce^{3+} luminescence is not observed, so the $4f^65d^1 \rightarrow 4f^7$ Eu^{2+} emission dominates the XEOL spectra –

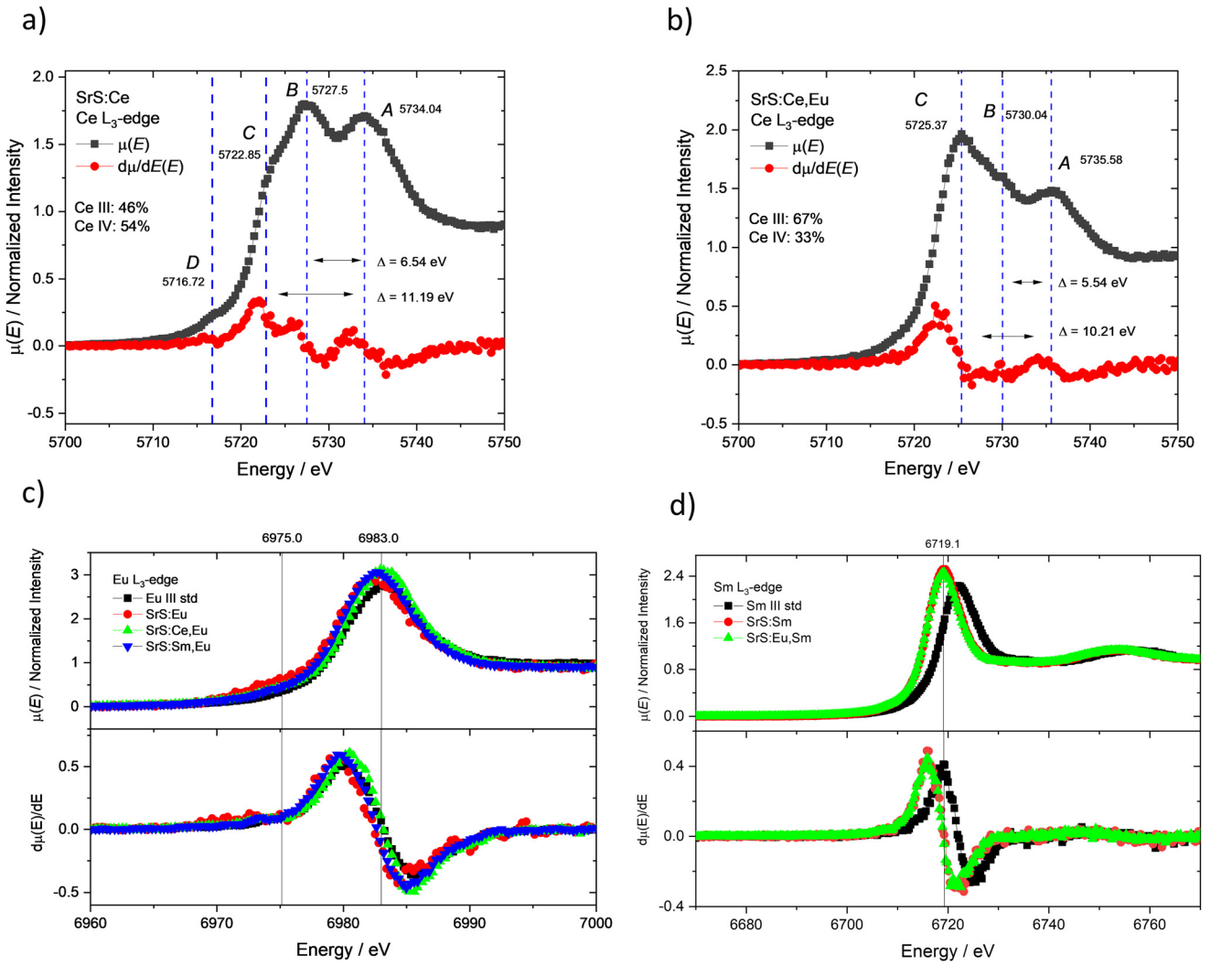

Fig. 5 XANES spectra for SrS materials and the associated derivatives at L_3-edges of (a and b) Ce, (c) Eu, and (d) Sm.

which also occurs for other X-ray excitation energies, as discussed later. The presence of Ce^{3+} as a co-dopant in SrS:Eu^{2+}, RE^{3+} materials is known to reduce the persistence of Eu^{2+} emission. The deeper energy levels of Ce^{3+} relative to the band structure of the SrS matrix favor the photoredox process, which then competes with trapping and de-trapping mechanisms in charge compensation defects. This competition may explain the diminished performance of SrS:Eu^{2+},Ce^{3+} as an energy storage material.

Variations of this mechanism have been proposed for other hosts and activator pairs,[38] in which *ab initio* calculations suggested that the wavelengths applied to induce the forward reaction are associated with a direct excitation of the metal-to-metal charge transfer (MMCT) band. In this regard, more experiments are needed to elucidate this hypothesis, in which it is considered that both forward and backward electron transfers occur through the host conduction band and are related to the persistent luminescent behavior in co-doped SrS materials. In this context, the presence of RE^{3+} co-dopants enhances defect formation through charge compensation but does not introduce new traps for persistent luminescence at room temperature. Another possibility for the increased Ce^{3+} population in SrS:Eu,Ce with respect to SrS:Ce is that Eu (Z = 63) has a higher X-ray absorption cross-section than Ce (Z = 58). Therefore, the energy of the Ce L_3-edge used in the excitation source favored the temporary oxidation of Eu^{2+} to Eu^{3+}, as a transition with a higher probability than $2p_{3/2} \rightarrow 5d$ of Ce. Indeed, all SrS materials exhibited a large amount of Eu^{3+}, demonstrated by the characteristic peak at 6979 eV. The presence of Eu^{2+} could be detected by a shoulder at 6972 eV, which is almost imperceptible for these samples. However, as described below, the emission spectra for Eu-doped strontium sulfide materials indicate the presence of the divalent ion, with a wide band centered in 610 nm, due to the strong interaction between 5d orbitals from Eu^{2+} and the sulfur ligands. In addition, as previously reported,[11] EPR experiments under blue light irradiation demonstrated the suppression of the Eu^{2+} signal, which indicated its photooxidation to the Eu^{3+}

ion, as proposed for the persistent luminescence mechanism in this material.

X-ray absorption spectra around the Sm L_3-edge (Fig. 5d) indicate only the presence of the Sm^{3+} ion, with the characteristic peak at 6719 eV, for all SrS materials. The absorption edge position of Sm in the Sm_2O_3 standard, however, exhibited a 3 eV shift, likely attributable to calibration discrepancies in the instrumentation. XANES measurements at the L_3-edges of rare earth dopants suggest, furthermore, that the process of reduction during the synthesis was more effective for Ce-doped materials than for Eu-doped SrS materials, despite the temporary ionization of Ce^{3+} and Eu^{2+} species by X-rays during the measurements. Divalent samarium species were also not detected, due to the lower Sm^{3+}/Sm^{2+} reduction potential (−1.55 eV (ref. 39)), even though CaS:Sm^{2+} and several Sm^{2+} doped phosphors are considerably stable.[40–42]

XANES and XEOL measurements were also recorded around the Sr L_3-edge and S K-edge to elucidate excitation and emission mechanisms (normalized curves, Fig. 6 and 7). The interaction of the X-rays with matter occurs mainly through three mechanisms, depending on the energy of the incident photons and on the atomic number of the absorber: the photoelectric effect, Compton scattering and pair production. The first one is predominant at low energies (below 100 keV); thus under the experimental conditions of this work, it is suitable to consider it as the main X-ray interaction mechanism. Photoionization of an atom by X-rays removes an inner shell electron from the atom, leaving behind a perturbed ion whose relaxation may take different routes, and may be accompanied by strong electronic effects.[43]

Around the Sr L_3-edge (Fig. 6a–c and 7a and b), it is seen that for all strontium sulfide materials, the X-ray induced luminescence decreases to a minimum at the edge (negative XEOL), which suggests that the optical luminescence and the X-ray absorption are competitive processes at Sr L_3. X-ray fluorescence and Auger emission are possible quenchers of luminescence under these conditions.[43]

For SrS:Sm^{3+} and SrS:Ce^{3+}, one can observe that the pre-edge region is associated with an increase in the luminescence intensity (positive XEOL), which does not occur for SrS:Eu^{2+}, SrS:Eu^{2+},Sm^{3+} and SrS:Eu^{2+},Ce^{3+} materials. The pre-edge transitions around the Sr L_3-edge may involve molecular orbitals as the final states, which are a mixture of Sr(3d) and S(3p) orbitals. Thus, the observed results for materials in which Eu^{2+} is the emission activator indicate that the luminescence mechanisms in these cases are not favored by Sr(2p) → Sr(3d)/S(3p) transitions, contrasting with the observed results for SrS:Ce^{3+} and SrS:Sm^{3+}, where the pre-edge region coincided with an intense maximum in the XEOL spectra. However, sample thickness is a crucial parameter that can also influence the pre-edge signal, primarily through self-absorption and non-linear absorption effects, potentially leading to misinterpretation of the data.

The XANES spectra at the sulfur K-edge (Fig. 6d–f and 7c, d) are very sensitive to the oxidation state with a range of 15 eV between reduced sulfur compounds (such as sulfides or metal complexes) and sulfur in the oxidation state +VI as sulfate. Furthermore, several types of sulfur compounds have a unique pattern of transitions on the absorption edge, which makes sulfur K-edge XANES very suitable to qualitatively determine

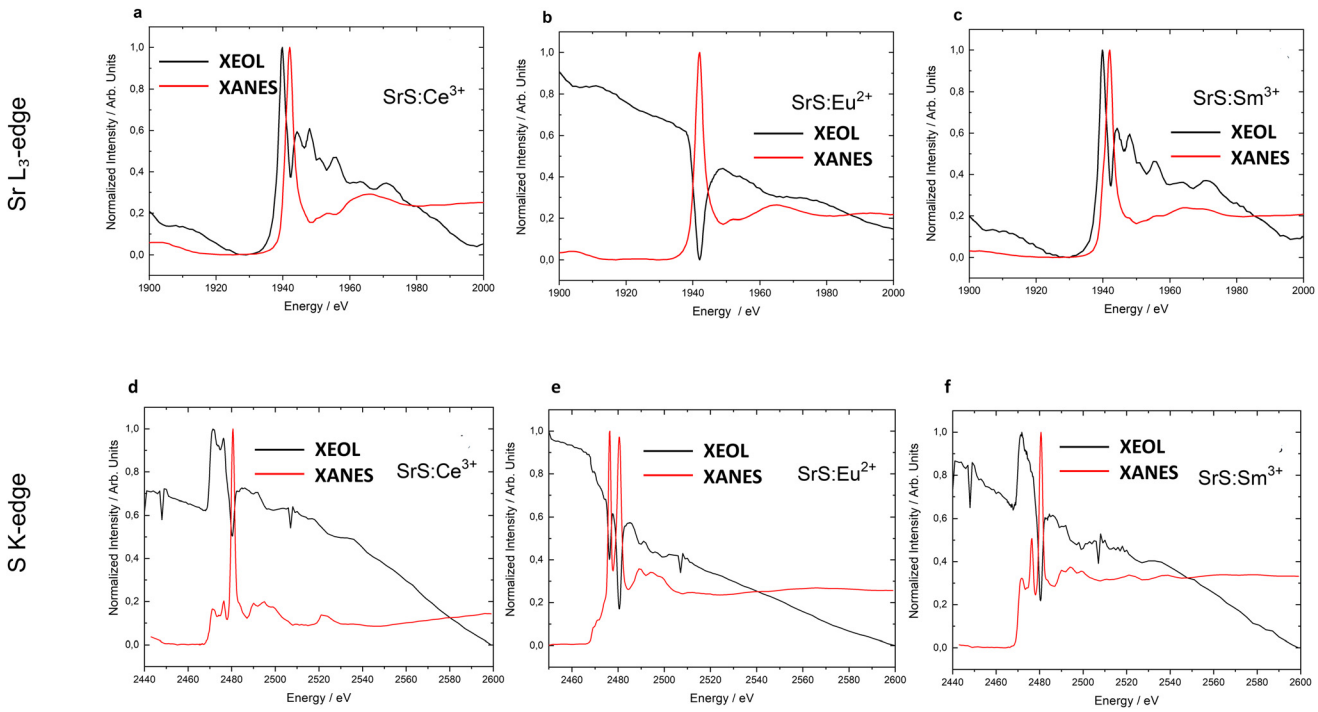

Fig. 6 XANES and XEOL spectra of single-doped SrS materials at the (a–c) Sr L_3-edge and (d–f) S K-edge.

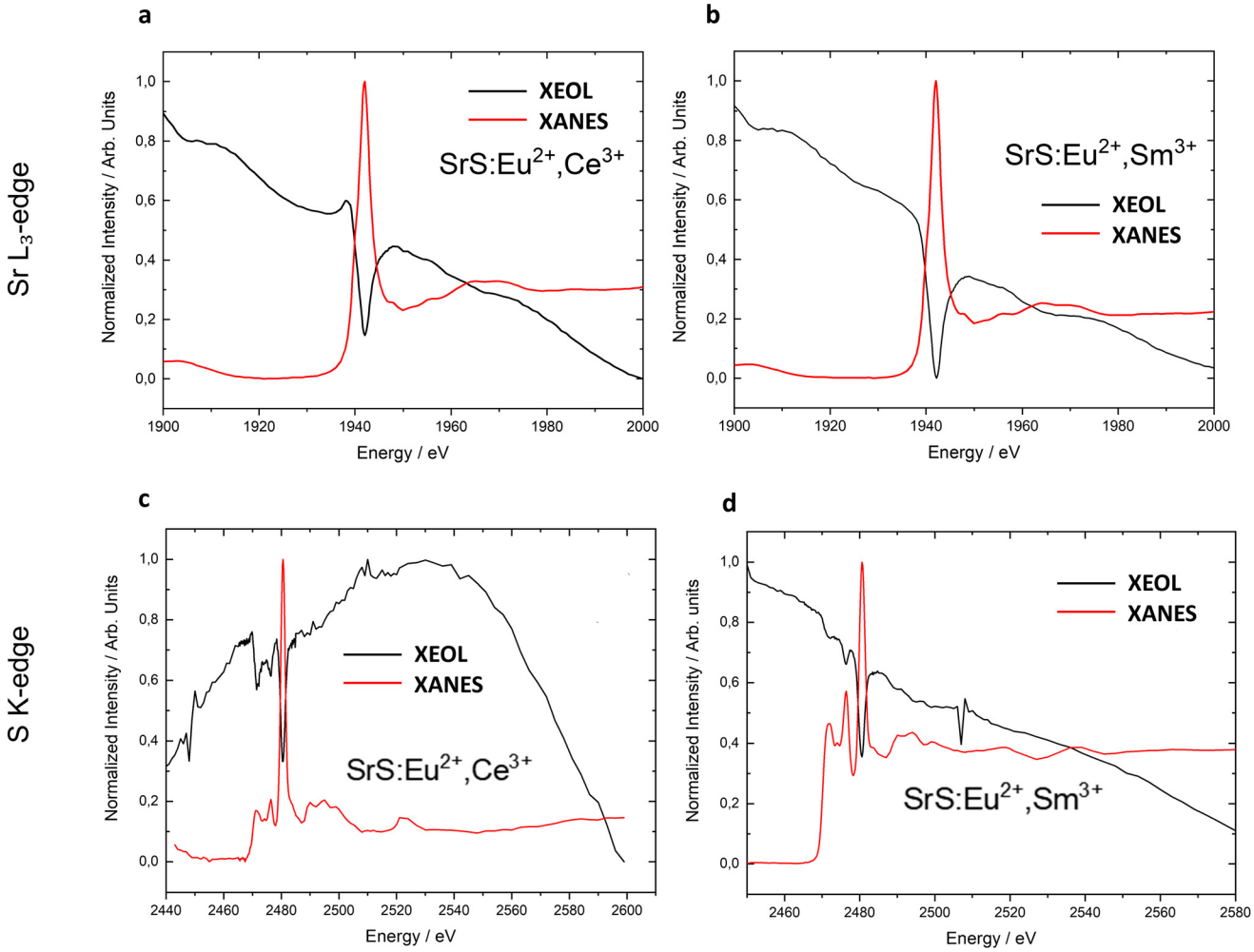

Fig. 7 XANES and XEOL spectra of co-doped SrS materials at the (a and b) Sr L_3-edge and (c and d) S K-edge.

the speciation of sulfur compounds in samples with simple or complex compositions.[44,45] For SrS materials, it can be considered that the observed edges at 2470 and 2482 eV are associated with S^{2-} and SO_4^{2-} species. Thus, around the S K-edge, it is seen that all strontium sulfide materials exhibited a negative XEOL at the sulfate edge, which is reasonable since $SrSO_4$ is an undesirable impurity and is not the emitting matrix. For SrS:Ce^{3+} and SrS:Sm^{3+} materials, the sulfide edge is associated with a positive XEOL, as expected for doped SrS, in which the sulfur oxidation state is −2. However, for strontium sulfide materials where Eu^{2+} is the activator center (SrS:Eu^{2+}, SrS:Eu^{2+}, Sm^{3+} and SrS:Eu^{2+},Ce^{3+}), even at the sulfide edge, a decrease in the X-ray induced luminescence is observed, thus indicating that the excitation at the sulfur K-edge leads to competitive processes instead of optical luminescence. The main reason for this – at first – unexpected behavior is the position of Eu^{2+} excited states related to the SrS band structure. The energy levels of Ce^{3+} and Sm^{3+} fundamental and first excited states are below that of Eu^{2+} and also inside the SrS bandgap. Thus, considering the discussed scintillation mechanism, the recombination step at the Eu^{2+} center is not favored once its $5d^1$ (e_g and t_{2g}) bands are overlapped with the SrS conduction band, where the electron secondary ionizations and other decay routes are possible under X-ray irradiation.

3.4 XEOL and X-ray induced persistent luminescence

The emission spectra of doped SrS materials provide a comparison between excitation at different energies (Sr L_3-edge and S K-edge). Fig. 8a shows the normalized emission spectra of SrS:Sm^{3+} under excitation at the pre-edge and post-edge and at the absorption edge of Sr and S. A wide band centered at 500 nm, related to the emission of defects, and also 4f–4f intraconfigurational Sm^{3+} transitions can be observed ($^4G_{5/2} \rightarrow {}^6H_J$, J = 5/2, 7/2, 9/2 and 11/2) at 515 nm, 600 nm, 650 nm and 700 nm. The emission spectra are all identical under different X-ray excitation energies; thus, it is possible to conclude that the X-ray absorption process interferes only with the intensity of luminescence if XEOL is positive or negative, but not with the energies of Sm^{3+} emissions. Emission spectra of SrS:Ce^{3+} are shown in Fig. 8b, along with the emission spectra of SrS:Eu^{2+} in Fig. 8c, which also remained unchanged under the different energies around Sr L_3 and S K-edges, corroborating

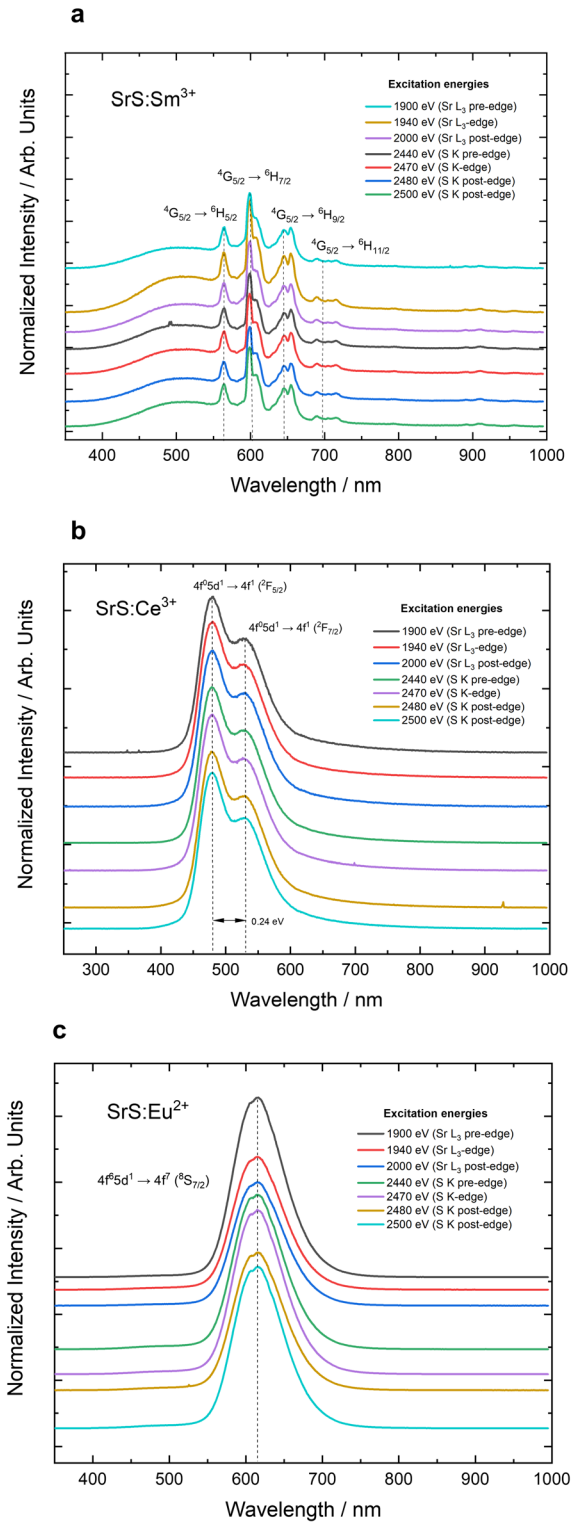

Fig. 8 XEOL spectra of rare earth doped strontium sulfide materials. (a) SrS:Sm^{3+}. (b) SrS:Ce^{3+}. (c) SrS:Eu^{2+}.

the hypothesis that the activation of the emitting ion with X-ray irradiation is not selective for the rare-earth transitions, acting only on the intensity of luminescence. Although XANES spectra indicated the presence of Eu^{3+}, the XEOL spectra of SrS:Eu^{2+} exhibit only $4f^65d^1 \rightarrow 4f^7$ Eu^{2+} emission, which is a wide band at 618 nm, redshifted by the nephelauxetic effect between Eu^{2+} 5d orbitals and sulfide ligands in the SrS matrix. The Eu^{3+}/Eu^{2+} reduction potential (−0.34 eV (ref. 39)) is, therefore, compatible with the reducing conditions applied in the synthesis process (ΔE° = 1.33 eV for CO (g) → CO_2 (g) reaction[46]). In Fig. S12,† the emission spectra of SrS:Eu^{2+},Ce^{3+} demonstrate, for all excitation energies, a wide band centered at 617 nm, related exclusively to $4f^65d^1 \rightarrow 4f^7$ Eu^{2+} emission, without the contribution of Ce^{3+} 4f–5d transitions, indicating an energy transfer mechanism, in which Ce^{3+} emission is suppressed by the presence of Eu^{2+} in the SrS matrix. Analogously, a suppression of Sm^{3+} 4f–4f transitions was observed for the SrS:Eu^{2+},Sm^{3+} material (Fig. S13†), whose emission spectra also show the wide $4f^65d^1 \rightarrow 4f^7$ Eu^{2+} emission band, for all X-ray excitation energies.

Fig. 9 shows the results of the study about X-ray induced persistent luminescence for the discussed materials around the S K-edge (2440, 2470, 2480 and 2550 eV excitation energies). The light output was registered while the samples were excited with X-rays for 300 seconds – charging phase, in which the emission intensity reaches its maximum – and also after the excitation source was switched off, in which a gradual decay – related to the release of charge carriers – was observed. It is possible to notice that all SrS materials presented persistent luminescence behavior under X-ray irradiation; however, no changes were observed in the luminescence decay curves with the different excitation energies, which indicates that the excitation mechanism remains the same at these regions. Despite the variations in total XEOL on S^{2-} and SO_4^{2-} absorption edges, as discussed, the increase or decrease in light emission probably refers only to emission intensity, and not to the electron trapping in the SrS materials. Furthermore, the high X-ray flux at the beamline results in the trapping processes occurring almost entirely, which become almost independent of the absorption cross section. Consequently, while the emission intensity is energy dependent, the persistent luminescence decay time remains unaffected.

Around the Sr L_3-edge, however, with excitation at the pre-edge, edge and post-edge regions, a decrease in persistent luminescence duration was observed when the materials were excited with energy equivalent to the L_3-edge (1940 eV), in which the luminescence decay is faster (Fig. 10). As shown in section 3.3, all SrS materials exhibited negative XEOL at this energy; therefore, this process negatively influences electron trapping, not only the light emission intensity. On comparing all SrS materials, when excited at both Sr L_3- and S K-edge regions, co-doped SrS:Eu^{2+},Sm^{3+} and SrS:Eu^{2+},Ce^{3+} materials exhibited longer persistent luminescence duration than single-doped SrS:Eu^{2+}, SrS:Sm^{3+} and SrS:Ce^{3+} materials, as occurs under excitation with visible and UV irradiation.

Despite the importance of crystal defects to persistent luminescence, EXAFS results did not demonstrate a clear correlation between the persistent luminescence decay time and the observed distortions in SrS structure. Among single-doped materials, SrS:Ce^{3+} exhibited the highest Debye–Waller and

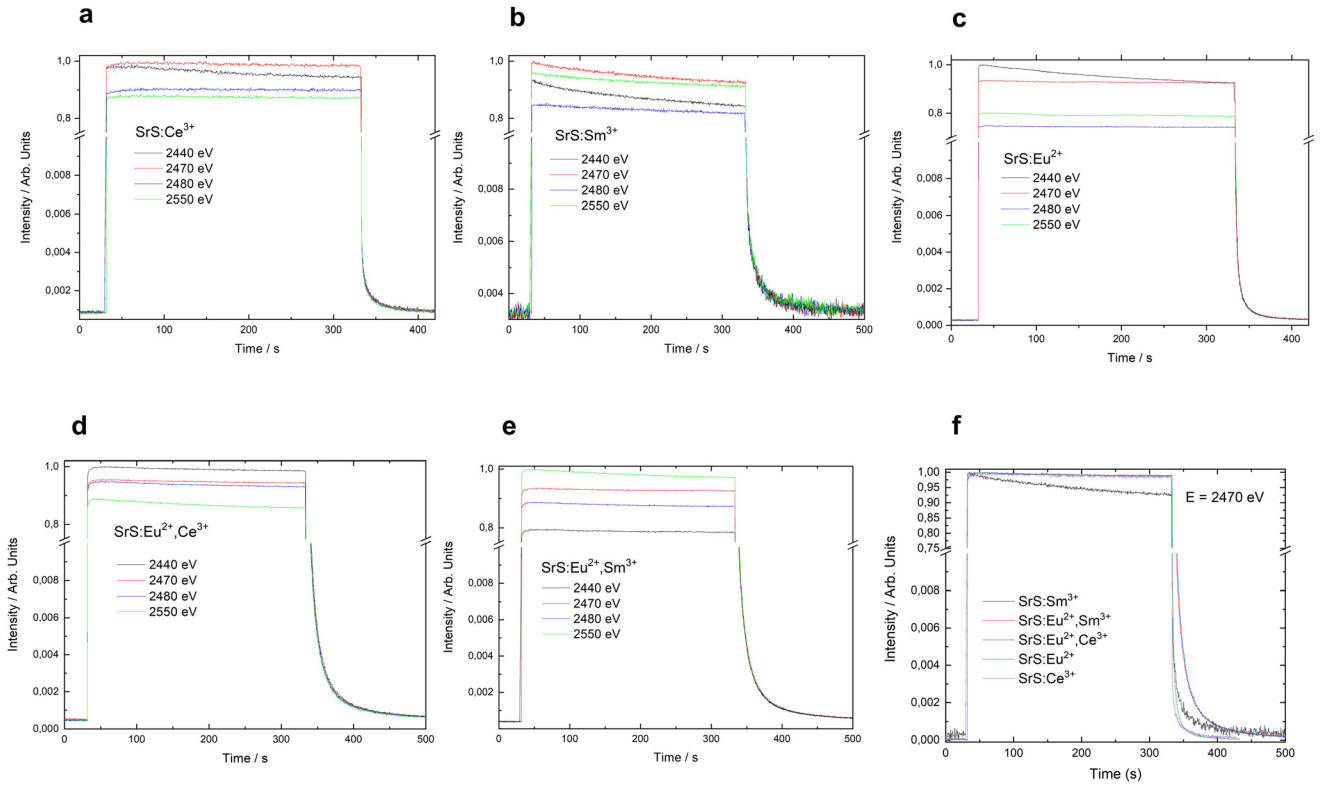

Fig. 9 Persistent luminescence decay after excitation at 2440, 2470, 2480 and 2550 eV (pre-edge, edge, and post-edge regions of S K) of SrS materials (co-) doped with (a) Ce^{3+}, b) Sm^{3+}, (c) Eu^{2+}, (d) Eu^{2+}, Ce^{3+} and (e) Eu^{2+}, Sm^{3+}. (f) Persistent luminescence decay after excitation at 2470 eV of all (co-) doped materials.

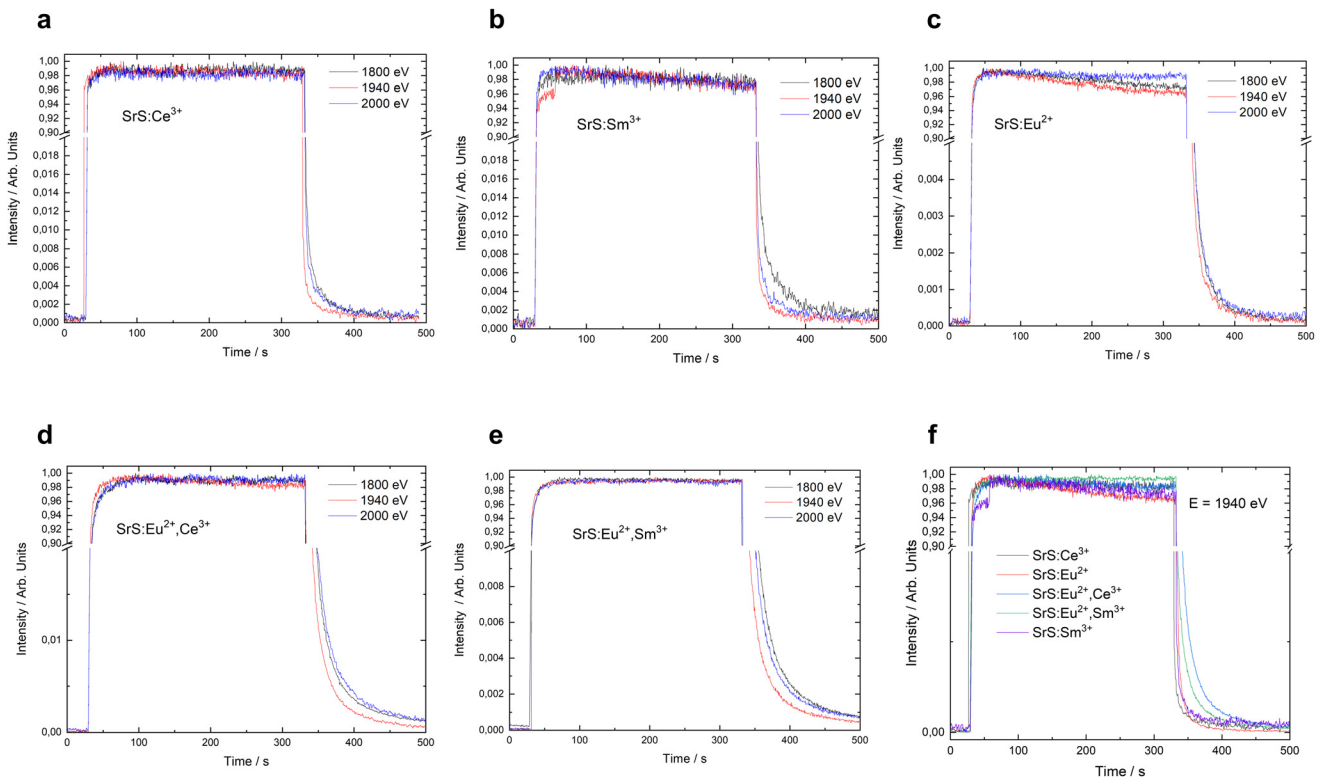

Fig. 10 Persistent luminescence decay after excitation at 1800, 1940 and 2000 eV (pre-edge, edge, and post-edge regions of Sr L_3) of SrS materials (co-) doped with (a) Ce^{3+}, (b) Sm^{3+}, (c) Eu^{2+}, (d) Eu^{2+},Ce^{3+} and (e) Eu^{2+},Sm^{3+}. (f) Persistent luminescence decay after excitation at 1940 eV of all (co-) doped materials.

alpha parameters – therefore, the most distorted structure with respect to the predicted SrS pure host – while SrS:Eu^{2+} emission persists longer under both UV and X-ray irradiation. SrS:Eu^{2+},Ce^{3+} is also the least efficient co-doped material, when compared with other SrS:Eu^{2+},RE^{3+} (RE: Sm, Er, Dy, Nd, Yb).[6] However, the persistent luminescent behavior is related to several factors, such as the quantity of defects in the crystal structure that may act as electron or hole traps, and also to the energy of the trap levels in the band structure. Therefore, it is not possible to assume that the structural disorder observed in EXAFS analysis for Ce-doped materials governs their photonic performance or is responsible for the decrease in persistent luminescence decay time.

As discussed, the creation of charge compensation defects should be the main effect of co-doping, so the $Ce^{3+/4+}$-co-doped material was supposed to exhibit a longer persistent luminescence decay time than SrS:Eu^{2+},Sm^{3+} – since in the first case, the also present tetravalent ion would induce a greater number of defects – which was not observed even with the structural changes induced by the incorporation of Ce^{3+}. In this context, it is possible to consider that the presence of both Ce^{3+} and Ce^{4+}, as probed by XANES, induces alternative paths for de-excitation, which negatively impacts the persistent luminescent behavior of Ce-doped SrS materials.

4. Conclusion

$RE^{2+/3+}$-doped SrS materials were synthesized with high yields through the microwave-assisted solid-state method. The observed sulfate and carbonate impurities did not exceed 10% in weight for most of the samples. In SR-XRD experiments, the incorporation of rare-earth dopants did not promote detectable structural changes in the SrS host. EXAFS analysis, however, demonstrated that when locally probing the environment around a Sr atom, considerable punctual changes were observed due to the replacement of some atoms in the structure by $RE^{2+/3+}$. Debye–Waller parameters and variations in bond lengths were quantitatively obtained for all materials. The direct correlation between the ionic radii differences and the disorder parameters illustrates the importance of the similarity of ionic radii in the substitutional process. The reliability of EXAFS fittings supports the hypothesis that the rare earth dopants are incorporated into the SrS structure as substitutional defects. In RE L_3-edge XANES spectra, it can be seen that both Ce^{3+} and Ce^{4+} species are present in SrS:Ce and SrS:Eu,Ce materials, and also that the population of trivalent Ce is increased by the presence of Eu^{2+} in SrS:Eu,Ce. X-ray irradiation promotes the temporary oxidation of Eu^{2+} and Ce^{3+} species during these measurements, which is related to the charging process in SrS persistent phosphors. By combining XEOL and XANES spectra at the Sr L_3 and S K-edges, the contribution of strontium and sulfur absorptions to the optical luminescence intensity was investigated. The XEOL emission spectra were identical under different X-ray excitation energies. In the case of SrS:Eu^{2+},Sm^{3+} and SrS:Eu^{2+},Ce^{3+} materials, only Eu^{2+} transition is observed, which indicates the occurence of energy transfer processes. Co-doped materials show longer persistent luminescence decay times in comparison with single-doped matrices, under excitation at both Sr L_3- and S K-edges, as a consequence of a greater number of defects. Distortions and bond disorder in the SrS crystal structure did not correlate with X-ray induced persistent luminescent behavior, which involves the competition between trapping and de-trapping processes, as well as the energy of trap levels as a result of rare-earth doping.

Data availability

The authors declare that all data underlying the results are available as part of the main article and the data supporting this article have been included as part of the ESI.† No additional source data are required.

Conflicts of interest

There are no conflicts to declare.

Acknowledgements

The authors are thankful for the financial support from FAPESP – São Paulo Research Foundation, Brazil (LCVR #2021/05603-1, #2021/08111-2 and #2022/11983-4; FAG #2019/25665-1; KTF scholarship #2019/26689-1) and CNPq – National Council for Scientific and Technological Development – Brazil (LCVR # 315126/2021-3). The authors also thank the Brazilian Center for Research in Energy and Materials – CNPEM for the measurements at the Brazilian Synchrotron Light Laboratory – LNLS (proposals 20170861-XRD1, 20170864-SXS, 20170868-XAFS2 and 20190093-XAFS2) and all the staff for the assistance during the experiments, especially Dr Flávio C. Vicentin, Dr Verônica C. Teixeira, Dr Santiago A. Figueroa, Dr Anna P. S. Sotero and Dr Alexandre M. Carvalho for their kind assistance.

References

1 V. Kolkovsky and R. Stübner, in *Metal Oxide Defects: Fundamentals, Design, Development and Applications*, ed. V. Kumar, V. Sharma, S. Som and H. Swart, Elsevier, Dresden, 2022, vol. 8, pp. 217–252.
2 L. Li, T. Li, Y. Hu, C. Cai, Y. Li, X. Zhang, B. Liang, Y. Yang and J. Qiu, *Light: Sci. Appl.*, 2022, **11**, 51.
3 E. Finley, M. W. Gaultois and J. Brgoch, *Phys. Chem. Chem. Phys.*, 2019, **21**, 19349–19358.
4 A. Feng, J. J. Joos, J. Du and P. F. Smet, *Phys. Rev. B*, 2022, **105**, 205101.
5 P. F. Smet, I. Moreels, Z. Hens and D. Poelman, *Materials*, 2010, **3**, 2834–2883.

6 A. Khare, S. Mishra, D. S. Kshatri and S. Tiwari, *J. Electron. Mater.*, 2017, **46**, 687–708.
7 Y. Yang, X. Li, X. Su, Z. Li, L. Liu, Y. Liu, J. Zhang, C. Mi and F. Yu, *Opt. Mater.*, 2014, **36**, 1822–1825.
8 W. Lian, Q. Yang, Y. Liu, D. Tu, L. Cai, X. Shang, B. Li, P. Hu, W. Zhang, Z. Chen and X. Chen, *Chem. Eng. J.*, 2024, **494**, 1385–8947.
9 Y. Kojima, A. Takahashi and T. Umegaki, *J. Lumin.*, 2014, **146**, 42–45.
10 M. Yazdanmehr, H. Sadeghi, M. K. Tehrani, S. J. Hashemifar and M. Mahdavi, *Opt. Mater.*, 2018, **75**, 304–313.
11 D. O. A. Dos Santos, L. Giordano, M. A. S. G. Barbará, M. C. Portes, C. C. S. Pedroso, V. C. Teixeira, M. Lastusaari and L. C. V. Rodrigues, *Dalton Trans.*, 2020, **49**, 16386–16393.
12 D. Van der Heggen, D. R. Cooper, M. Tesson, J. J. Joos, J. Seuntjens, J. A. Capobianco and P. F. Smet, *Nanomaterials*, 2019, **9**, 1127.
13 P. Pei, Y. Chen, C. Sun, Y. Fan, Y. Yang, X. Liu, L. Lu, M. Zhao, H. Zhang, D. Zhao, X. Liu and F. Zhang, *Nat. Nanotechnol.*, 2021, **16**, 1011–1018.
14 C. Richard and B. Viana, *Light: Sci. Appl.*, 2022, **11**, 123.
15 Y. Zhuang, D. Chen, W. Chen, W. Zhang, X. Su, R. Deng, Z. An, H. Chen and R. Xie, *Light: Sci. Appl.*, 2021, **10**, 132.
16 X. Chen, J. Song, X. Chen and H. Yang, *Chem. Soc. Rev.*, 2019, **48**, 3073–3101.
17 L. Song, P. Li, W. Yang, X. Lin, H. Liang, X. Chen, G. Liu, J. Li and H. Yang, *Adv. Funct. Mater.*, 2018, **28**, 1707496.
18 Y. Fan, P. Wang, Y. Lu, R. Wang, L. Zhou, X. Zheng, X. Li, J. A. Piper and F. Zhang, *Nat. Nanotechnol.*, 2018, **13**, 941–946.
19 B. D. Fairbanks, L. J. Macdougall, S. Mavila, J. Sinha, B. E. Kirkpatrick, K. S. Anseth and C. N. Bowman, *Chem. Rev.*, 2021, **121**, 6915–6990.
20 M. V. D. S. Rezende, P. J. R. Montes, A. B. Andrade, Z. S. Macedo and M. E. G. Valerio, *Phys. Chem. Chem. Phys.*, 2016, **18**, 17646–17654.
21 A. M. G. Carvalho, D. H. C. Araujo, H. F. Canova, C. B. Rodella, D. H. Barrett, S. L. Cuffini, R. N. Costa and R. S. Nunes, *J. Synchrotron Radiat.*, 2016, **23**, 1501–1506.
22 B. H. Toby and R. B. Von Dreele, *J. Appl. Crystallogr.*, 2013, **46**, 544–549.
23 S. J. A. Figueroa, J. C. Mauricio, J. Murari, D. B. Beniz, J. R. Piton, H. H. Slepicka, M. Falcao de Sousa, A. M. Espindola and A. P. S. Levinsky, *J. Phys.: Conf. Ser.*, 2016, **712**, 012022.
24 H. Tolentino, V. Compagnon-Cailhol, F. C. Vicentin and M. Abbate, *J. Synchrotron Radiat.*, 1998, **5**, 539–541.
25 B. Ravel and M. Newville, *J. Synchrotron Radiat.*, 2005, **12**, 537–541.
26 J. M. Carvalho, C. C. S. Pedroso, I. P. Machado, J. Hölsä, L. C. V. Rodrigues, P. G. Głuchowski, M. Lastusaari and H. F. Brito, *J. Mater. Chem. C*, 2018, **6**, 8897–8905.
27 A. A. Khan and V. T. Deshpande, *Acta Crystallogr., Sect. A*, 1968, **24**, 402–402.
28 K. Burger, D. Cox, R. Papoular and W. Prandl, *J. Appl. Crystallogr.*, 1998, **31**, 789–797.
29 S. M. Antao and I. Hassan, *Can. Mineral.*, 2009, **47**, 1245–1255.
30 B. Qu, B. Zhang, L. Wang, R. Zhou and X. C. Zeng, *Chem. Mater.*, 2015, **27**, 2195–2202.
31 T. Aitasalo, J. Hassinen, J. Hölsä, T. Laamanen, M. Lastussari, M. Malkamäki, J. Niittykoski and P. Novák, *J. Rare Earths*, 2009, **27**, 529–538.
32 R. D. Shannon, *Acta Crystallogr., Sect. A*, 1976, **32**, 751–767.
33 L. Zhang and S. Li, *Phys. B*, 2014, **434**, 38–43.
34 D. Raoux, *Z. Phys. B: Condens. Matter*, 1985, **61**, 397–403.
35 J. Hu, Z. Yang, A. Feng, R. V. Deun, P. F. Smet and D. Van der Heggen, *J. Phys. Chem. C*, 2022, **126**, 21396–21404.
36 A. V. Soldatov, T. S. Ivanchenko, S. Della Longa, A. Kotani, Y. Iwamoto and A. Bianconi, *Phys. Rev. B: Condens. Matter Mater. Phys.*, 1994, **50**, 5074–5080.
37 A. Bianconi, A. Marcelli, H. Dexpert, R. Karnatak, A. Kotani, T. Jo and J. Petiau, *Phys. Rev. B: Condens. Matter Mater. Phys.*, 1987, **35**, 806–812.
38 J. J. Joos, I. Neefjes, L. Seijo and Z. Barandiarán, *J. Chem. Phys.*, 2021, **154**, 064704.
39 S. Cotton, *Lanthanide and Actinide Chemistry*, Wiley, 2006, pp. 1–263.
40 J. Zhang, Y. Fan, Z. Chen, S. Yan, J. Wang, P. Zhao, B. Hao and M. Gai, *J. Rare Earths*, 2015, **33**, 922–926.
41 C. van Aarle, N. Roturier, D. A. Biner, K. W. Krämer and P. Dorenbos, *Opt. Mater.*, 2023, **145**, 114375.
42 G. J. Odendaal, L. J. B. Erasmus, R. E. Kroon and H. C. Swart, *Phys. B*, 2023, **669**, 415319.
43 F. de Groot and A. Kotani, *Core level spectroscopy of solids. Core Level Spectroscopy of Solids*, CRC Press, 2008, pp. 1–491.
44 G. Almkvist, K. Boye and I. Persson, *J. Synchrotron Radiat.*, 2010, **17**, 683–688.
45 M. E. Fleet, X. Liu, S. L. Harmer and P. L. King, *Can. Mineral.*, 2005, **43**, 1605–1618.
46 J. Rumble, *CRC Handbook of Chemistry and Physics*, CRC Press, 100th edn, 2019.